

Physics-based model reconciles caldera collapse induced static and dynamic ground motion: application to Kīlauea 2018

Taiyi Wang¹, Katherine Coppess², Paul Segall¹, Eric M. Dunham^{1,3}, William Ellsworth¹

¹Department of Geophysics, Stanford University

²Department of Physics, Stanford University

³Institute of Computational and Mathematical Engineering, Stanford University

Key Points:

- Caldera block/magma momentum change and chamber pressurization parsimoniously explain co-collapse inflation and very long period events
- Coupled tri-axial expansion source and vertical single force arise in the point source limit, contributing to very long period waveforms
- Inversion constrains co-collapse shear strength drop, pressurization, and mass of caldera block/magma during Kīlauea's 2018 events

Abstract

Inflationary deformation and very long period (VLP) earthquakes frequently accompany basaltic caldera collapses, yet current interpretations do not reflect physically consistent mechanisms. We present a lumped parameter model accounting for caldera block/magma momentum change, magma chamber pressurization, and ring fault shear stress drop. The effect of pressurizing a spheroidal chamber is represented as a tri-axial expansion source, and the combined caldera block/magma momentum change as a vertical single force. The model is applied to Kīlauea 2018 caldera collapse events, accurately predicting near field static/dynamic ground motions. In addition to the tri-axial expansion source, the single force contributes significantly to the VLP waveforms. For an average collapse event with fully developed ring fault, Bayesian inversion constrains ring fault stress drop to ~ 0.4 MPa and the pressure increase to ~ 1.7 MPa. That the predictions fit both geodetic and seismic observations confirms that the model captures the dominant caldera collapse mechanisms.

Plain Language Summary

Episodic caldera collapses at basaltic volcanoes can be hazardous, and forecasting them requires correct interpretations of geophysical observations. We use a physics-based approach to explain caldera collapse induced ground motions, such as during the 2018 collapse of Kīlauea. We show that, the most fundamental physical mechanisms of caldera collapse involve a pressure increase in the underlying magma chamber, due to rapid reduction of its volume, and a time-varying force, due to the acceleration of caldera block/magma. The physics-based model will allow more accurate interpretations of seismic data collected from less well monitored caldera collapses.

Corresponding author: Taiyi Wang, taiyi@stanford.edu

39 1 Introduction

40 A major challenge in understanding episodic caldera collapse at basaltic shield vol-
 41 canoes is relating geophysical observations to the collapse dynamics. Inflationary co-collapse
 42 deformation outside of collapsing calderas (e.g., Michon et al., 2009; Segall et al., 2020),
 43 recorded by Global Navigation Satellite Systems (GNSS) or tiltmeters, and very long pe-
 44 riod (VLP) events (e.g., Kumagai et al., 2001; Fontaine et al., 2019), captured by seis-
 45 mometers, are reported at nearly all basaltic caldera collapses. Separate analyses of co-
 46 collapse deformation and VLP events have led to significant insight into caldera collapse
 47 dynamics (Kumagai et al., 2001; Gudmundsson et al., 2016; Duputel & Rivera, 2019; Ro-
 48 man & Lundgren, 2021; Segall & Anderson, 2021). However, geodetic data often do not
 49 have the temporal resolution to capture transient dynamics of caldera collapse, and their
 50 interpretations have been limited to kinematic magma chamber-ring fault interactions.
 51 In contrast, VLP waveforms are typically analyzed with moment tensor inversions, which
 52 do not lead to unique physical interpretations, absent constraints from near-field geode-
 53 tic observations. Because of these limitations, current interpretations of co-collapse static
 54 and dynamic ground motions do not reflect mutually-consistent caldera collapse dynam-
 55 ics. Understanding the underlying dynamics would aid in interpreting cases where only
 56 seismic data are available, and aid in forecasting future collapse behavior.

57 Simultaneous analyses of GNSS/tilt and VLP data can shed light on caldera col-
 58 lapse dynamics by including observations over a wide range of time (seconds to minutes)
 59 and spatial (near-field to regional) scales. A predictive model capable of simulating both
 60 static and dynamic ground motions is required for such analyses. Kumagai et al. (2001)
 61 first introduced a quantitative model to explain the inflationary deformation associated
 62 with caldera collapses at Miyakejima. More recent models build on Kumagai et al. (2001)’s
 63 effort to include rate-and-state friction on the ring fault (Segall & Anderson, 2021) and
 64 to describe the dynamics of collapse sequences (Roman & Lundgren, 2021). We aim to
 65 add additional physics to the dynamic model and provide a parsimonious explanation
 66 of co-collapse static/dynamic ground motion.

67 Here we extend the Kumagai et al. (2001) model to account for the momentum change
 68 of magma, which is accelerated by the rapid downward movement of the collapsing caldera
 69 block. We present analytical solutions for caldera block displacement, chamber pressure,
 70 and ring fault shear stress as a function of time. We then formulate pressure and shear
 71 stress changes as a time-varying tri-axial expansion source and a single force. For the
 72 expansion source, we utilize a moment tensor form consistent with spheroidal cavities
 73 of any aspect ratio under uniform pressurization (Eshelby, 1957). Lastly, we apply the
 74 proposed model in a joint inversion of co-collapse GNSS displacement offsets and VLP
 75 velocity waveforms to gain insight into Kilauea’s 2018 caldera collapse events.

76 2 Theory

77 2.1 A model for caldera collapse dynamics

78 Consider a caldera block idealized as a cylindrical “piston” with radius R , height
 79 L , and bulk density ρ_p (Fig. 1 a). Prior to a collapse event, the piston is in static equi-
 80 librium, where the gravitational force, F_g , is balanced by magma chamber pressure force
 81 at the bottom of the piston, F_p , and the shear force on the ring fault, F_s . For basaltic
 82 shield volcanoes, flank eruptions reduce chamber pressure, thereby increasing shear stress
 83 on the ring fault leading to collapse. When shear stress on the ring fault exceeds the static
 84 strength, collapse initiates. The caldera block accelerates downwards, resulting in a force
 85 of equal magnitude to its momentum change, but of opposite direction (upward) on the
 86 crust. The collapsing caldera rapidly reduces the chamber volume, pressurizing the un-
 87 derlying magma chamber. The pressure force on the caldera block then increases, which
 88 decelerates the caldera block. A deceleration is equivalent to an upward acceleration of

89 the caldera block. Therefore, past the peak downward velocity, the net force on the crust
 90 points downwards. Eventually, when the caldera block arrests, static equilibrium is re-
 91 stored.

Assuming rigid body motion of the piston, and a surrounding stationary, rigid crust, the momentum balance for the piston is:

$$\begin{aligned} m\ddot{u} &= F_g + F_s + F_p \\ &= mg - (2\pi RL)\tau(t) - (\pi R^2)p(t) \end{aligned} \quad (1)$$

where the left hand side is piston momentum change, u is the time dependent displacement and over-dot indicating time derivatives. The mass of the piston is $m = \pi R^2 L \rho_p$. τ is the spatially averaged shear stress on the side of the piston and p is the chamber pressure at its bottom. Note that $p(t) = p_0 + \delta p(t)$, where p_0 is the background pressure (prior to collapse) and δp the perturbation due to collapse. Due to the short duration of collapse events, the change in magma mass during collapse is neglected. Also neglecting acoustic waves and tractions due to viscous flow, the co-collapse chamber pressure evolution including chamber storativity and magma momentum change is (Appendix A):

$$p = \frac{\pi R^2}{\beta V} u + \frac{\phi m_f}{\pi R^2} \frac{\partial^2 u}{\partial t^2} + p_0 \quad (2)$$

92 where β is total compressibility (chamber + magma), V chamber volume, ϕm_f the
 93 inertial mass of magma in the chamber. Eqn. 2 is based on an asymptotic expansion of
 94 the solution in powers of the small parameter $\omega H/c$, where ω is the angular frequency,
 95 H is the characteristic length scale of the chamber, and c the acoustic wave speed of the
 96 magma. The zeroth order effect is that of pressurization due to storage properties of the
 97 chamber. We also account for inertia of the magma, an effect that is second order in $\omega H/c$.

For a cylindrical chamber of the same radius as the piston, $\phi = 1/3$ (Eqn. A6). For spheroidal chambers, $\phi < 1/3$. Substituting Eqn. 2 into the momentum balance yields:

$$m'\ddot{u} + \frac{\pi^2 R^4}{\beta V} u = mg - (2\pi RL)\tau - (\pi R^2)p_0 \quad (3a)$$

$$m' = m + \phi m_f \quad (3b)$$

The inertia imparted by magma within the chamber acts as an extra mass added to the piston (Fig. 1 c). We employ simple static-dynamic friction:

$$\tau_{str} = f\sigma_n \quad (4a)$$

$$f = \begin{cases} f_s & \dot{u} = 0 \\ f_d & \dot{u} > 0 \end{cases} \quad (4b)$$

where σ_n is the spatially averaged effective normal stress on the ring fault. Once the piston starts moving at $t = 0$, the strength, τ_{str} , instantaneously drops from the static strength, $\tau_{str}^s = f_s\sigma_n$, to the dynamic strength, $\tau_{str}^d = f_d\sigma_n$. The co-collapse displacement $u(t)$ and perturbation pressure $\delta p(t)$ are found analytically, assuming $\tau = \tau_{str}^d$ for $0 < t < t_{max}$ (Eqn. B3b and Fig. 1 c). The shear stress change for $0 \leq t \leq t_{max}$, assuming zero acceleration at $t = 0, t_{max}$ is thus:

$$\delta\tau = (-\pi R^2 \delta p - m'\ddot{u})/(2\pi RL). \quad (5)$$

98 2.2 Point source representation

99 We seek a point source representation of the caldera collapse dynamics, which en-
 100 ables forward predictions of associated ground motion. A point source representation is

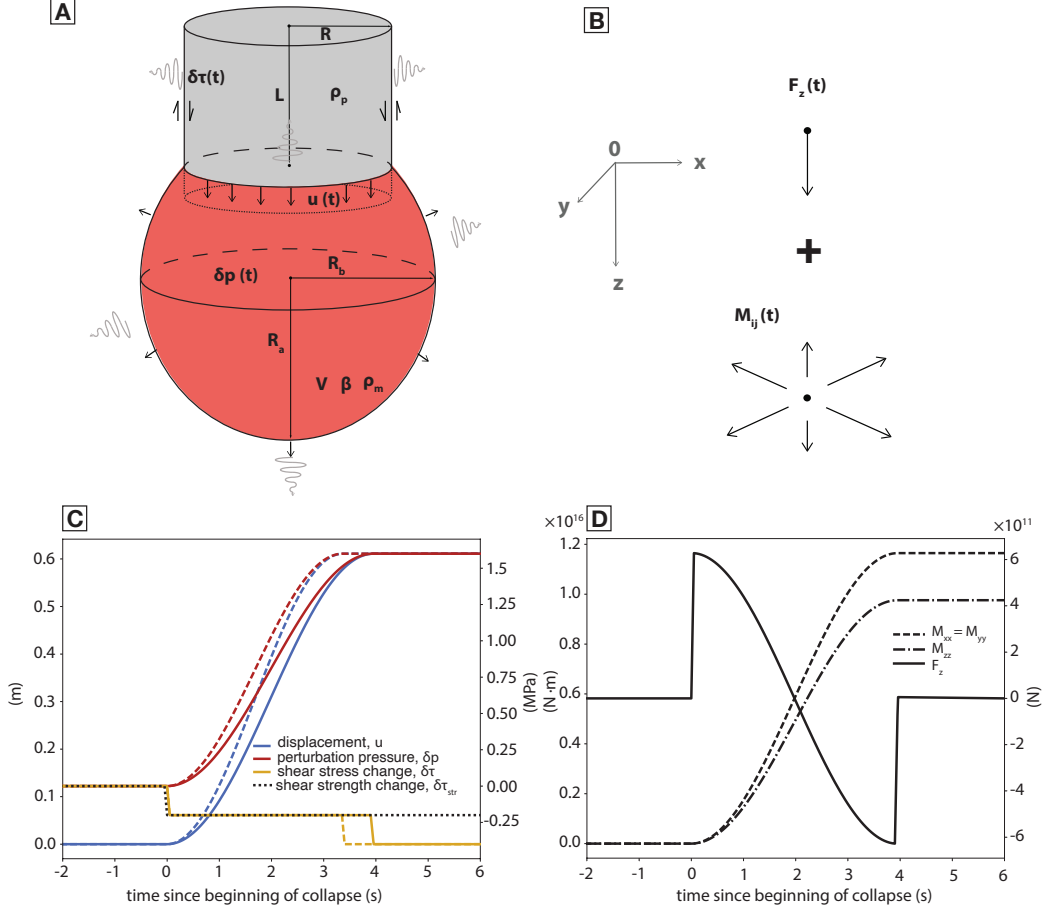


Figure 1: (a) Schematic of the caldera collapse model. Collapse block is idealized as an axially-symmetric piston bounded by a vertical ring fault. A vertically oriented, spheroidal chamber of aspect ratio α ($\alpha > 1$, prolate, $\alpha < 1$, oblate) is comprised of homogeneous, compressible magma bounded by elastic crust. (b) Coordinate system and the point source representation. Positive z axis points downward. $z = 0$ marks the piston bottom prior to collapse. Piston/magma momentum change and chamber pressurization are represented as a vertical single force and a point tri-axial pressure source, respectively. (c) Example solution to the momentum and mass balance equations. Solid lines show displacement, perturbation pressure, and shear stress, accounting for magma momentum change, which lengthens the collapse duration. Dashed lines show solutions without accounting for magma momentum change. Total shear stress drop is twice that of shear strength drop. (d) Corresponding time-dependent moment tensor components and vertical single force, for a chamber aspect ratio $\alpha > 1$.

101 justified when the wavelengths considered are long compared to source dimensions. As-
 102 suming a s-wave velocity of 3 km/s, the wavelength of typical VLP events, which have
 103 duration of ~ 5 seconds, is of order $5 \text{ s} \times 3 \text{ km/s} = 15 \text{ km}$, whereas the effective di-
 104 mension of the source (basaltic magma chamber and piston) is $\sim 2 \text{ km}$. We thus use
 105 a tri-axial expansion point source to represent the pressure perturbation exerted on the
 106 magma chamber wall, and a vertical single force to represent the reaction force on the
 107 crust.

108 Pressurization of a spheroidal magma chamber can be represented by a tri-axial
 109 expansion source with moment tensor components, M_{ij} , which are derived by solving
 110 a system of equations involving the chamber aspect ratio, α , volume, V , and the pres-
 111 sure change, δp , given shear modulus μ and Poisson's ratio ν (Eshelby, 1957; Davis, 1986).
 112 Unbalanced forces give rise to momentum change, which is represented as a single force
 113 in the point source limit. The single force on the crust is of equal magnitude and oppo-
 114 site direction to the single force on the combined piston and magma mass, $F_z = -m'\ddot{u}$.

The dynamic displacement field is then computed by convolving the moment ten-
 sor, M_{ij} , and the vector single force, F_i , with the elastodynamic Green's functions G_{ij} :

$$u_i(\mathbf{x}, t) = \int_0^t M_{jk}(\mathbf{x}_0, t_0) \frac{\partial G_{ij}(\mathbf{x}_0, \mathbf{x}, t - t_0)}{\partial (\mathbf{x}_0)_k} dt_0 + \int_0^t F_i(\mathbf{x}_0, t_0) G_{ij}(\mathbf{x}_0, \mathbf{x}, t - t_0) dt_0 \quad (6)$$

115 where $i = x, y$ or z . \mathbf{x}_0, t_0 denote the source location and time, whereas \mathbf{x}, t denote
 116 the receiver location and time. Here $F_i = [0, 0, F_z]$. The static limit of the dynamic dis-
 117 placements for various chamber aspect ratios is verified (Fig. S3) using the semi-analytical
 118 Yang-Cervelli model (Yang et al., 1988; Cervelli, 2013).

119 3 Application to the 2018 collapse of Kīlauea caldera

120 3.1 GNSS and seismic data

121 We analyze near-field, co-collapse displacement offsets and VLP waveforms asso-
 122 ciated with the last 32 (of 62 total) collapse events, which are broader in scale, and oc-
 123 curred along a relatively well developed ring fault system. We use the displacement off-
 124 sets and uncertainties computed by Segall et al. (2020). Offsets are determined as the
 125 difference between GNSS averaged positions (5 s solutions, stacked over 32 events) be-
 126 fore and after a collapse event. We used a selection of 3 accelerometers (HMLE, PAUD,
 127 and RSDD) maintained by the National Strong Motion Project and 3 broadband seis-
 128 mometers (MLOD, HLPD, and STCD) maintained by the Hawaii Volcano Observatory
 129 for VLP waveform analyses (Fig. 2 a). For the accelerometers, we stack the waveforms
 130 from each component for the last 32 events, deconvolve the instrument response, inte-
 131 grate to velocity, and low-pass filter at a period of 5 seconds. Broadband velocity wave-
 132 forms were processed similarly without integration in time.

133 3.2 Velocity model

134 We adopt a homogeneous half-space model of Kīlauea, assuming a s-wave veloc-
 135 ity of $c_s = 1 \text{ km/s}$, a p-wave velocity of $c_p = 1.7 \text{ km/s}$, and an extra-caldera crustal
 136 density of $\rho_c = 3000 \text{ kg/m}^3$ (justification in Section S3). Green's functions are gener-
 137 ated using the FK method (Zhu & Rivera, 2002). Co-collapse displacement offsets are
 138 obtained by taking the limit $t \rightarrow \infty$.

139 3.3 Bayesian inversion

We employ a Bayesian framework to estimate the posterior probability density func-
 tion (PDF) of the model parameters $\Delta\tau_{str}$, V , β , ρ_p , $\phi\rho_f$, R , and α , while fixing the depth
 and centroid location of the underlying Halema'uma'u chamber to the median estimate

Parameters	Symbol	Unit	Bounds on the uniform portion of prior	MAP model	90% confidence interval
In inversion					
shear strength drop	$\Delta\tau_{str}$	MPa	[0.1, 1.3]	0.19	[0.19, 0.21]
piston radius	R	km	[0.5, 1.3]	0.45	[0.38, 0.57]
chamber volume	V	km ³	[2.5, 7.2]	4.6	[3.4, 7.2]
total compressibility	β	Pa ⁻¹	[10 ^{-9.70} , 10 ^{-8.88}]	10 ^{-9.73}	[10 ^{-9.81} , 10 ^{-9.53}]
piston density	ρ_p	kg · m ⁻³	[2400, 2800]	2500	[2350, 2820]
effective magma density	$\phi\rho_f$	kg · m ⁻³	[210, 870]	170	[30, 260]
chamber aspect ratio ¹	α	-	[1.0, 1.4]	0.88	[0.88, 0.89]
Fixed					
crustal shear modulus	μ	GPa	3	-	-
Poisson's ratio	ν	-	0.25	-	-
crustal density outside of caldera	ρ_c	kg · m ⁻³	3000	-	-

¹ $\alpha > 1$ and $\alpha < 1$ indicate prolate and oblate, respectively.

Table 1: Model parameters, bounds on the uniform portion of prior, MAP model, and 95% confidence interval. The chamber centroid is fixed at the following longitude, latitude, and depth from surface: 155.278 °W , 19.407 °N, 1.94 km. Piston height, L , is defined as the depth to chamber centroid, subtracting chamber semi-major axis length.

of Anderson et al. (2019) (Table 1, also discussion in Section S5):

$$P(\mathbf{m}|\mathbf{d}) \propto P(\mathbf{d}|\mathbf{m})P(\mathbf{m}) \quad (7)$$

where \mathbf{m} denotes model parameters and \mathbf{d} the data. This equation states that the probability of a model conditioned on data, $P(\mathbf{m}|\mathbf{d})$ (posterior), is proportional to the product of the likelihood, $P(\mathbf{d}|\mathbf{m})$, and the prior distribution of the model parameters, $P(\mathbf{m})$. We employ a Gaussian-tailed uniform prior distribution (Table 1), where the standard deviation of the tail is 1/10 the width of the uniform part of the distribution (Anderson & Poland, 2016). The posterior probability density function (PDF) is estimated by an affine-invariant ensemble sampler for Markov Chain Monte Carlo (MCMC) (Foreman-Mackey et al., 2013). A detailed discussion on choice of covariance matrices can be found in Section S7.

Models were restricted to those with a collapse duration of 2–8 seconds, ring fault slip of 2–5 meters, and pressure increase of 0.5–4 MPa. A pressure increase of 1–3 MPa was estimated by Segall et al. (2020). GNSS station CALS, located on the caldera block, indicates 2.4 ± 0.4 m of co-collapse slip during a 5 – 10 s period (Segall & Anderson, 2021). In trial inversions, magma momentum change appears to be of minor importance compared to that of caldera block, so we only used caldera block momentum change in generating forward predictions of the single force induced ground motions.

3.4 Results

The maximum a-posteriori (MAP) model not only generates predictions consistent with the duration and magnitude of the collapse, but also explains 67% of the variance in the static displacements and 64% of the variance in the VLP velocity waveforms (Fig. 2 b, c). Over-prediction of vertical static displacement is consistent with an oblate chamber geometry (discussed in Section 4.3). The fit to waveform relative phase amplitude is rather good, with exceptions at station HLPD and MLOD, which may be due to unaccounted-

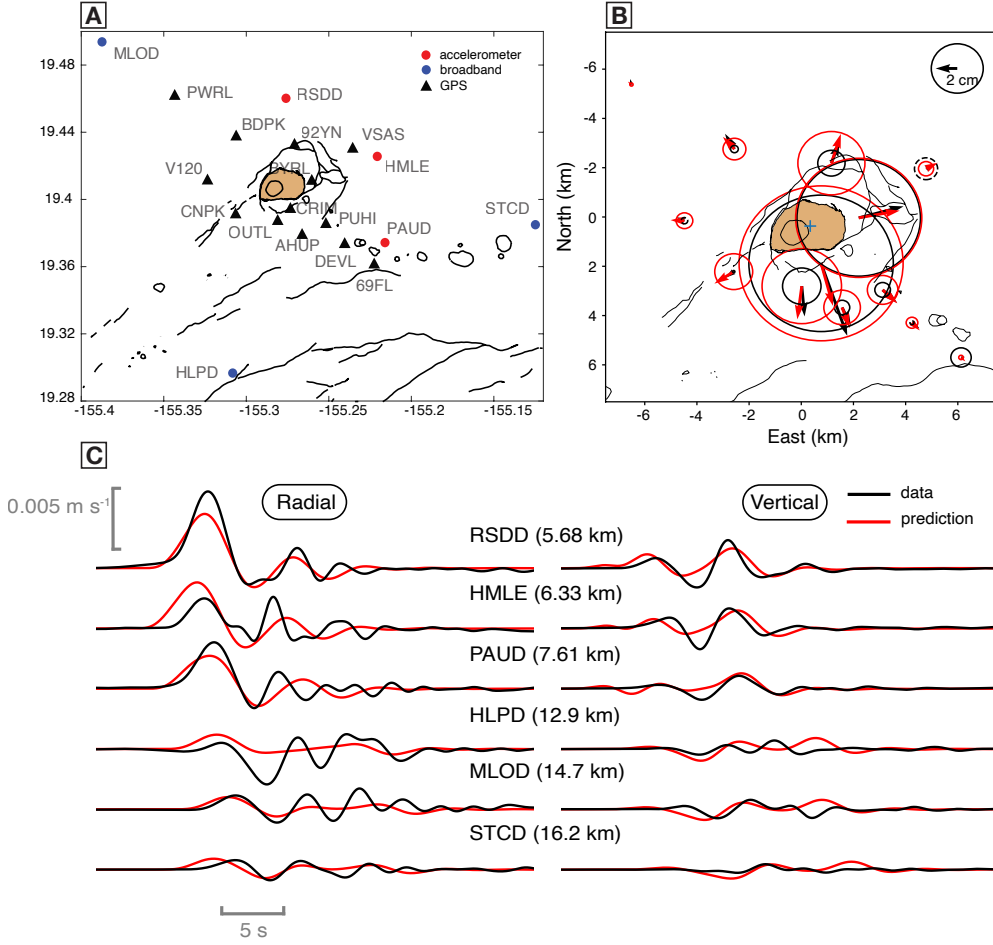


Figure 2: Comparison of observed and predicted static displacement and dynamic velocity waveform. (a) Map of accelerometers, broadband seismic stations, and permanent GNSS stations at Kilauea summit, with pre-collapse caldera boundary. 2018 collapse structure is shaded. (b) fit to the GPS data with Maximum a-posterior (MAP) model, with radial component in arrows and vertical component in circles. Blue cross marks the location of Halema'uma'u chamber centroid. (c) fit to the VLP velocity wave forms low pass-filtered at 5 s.

163 for elastic heterogeneities. The MAP model (Table 1) corresponds to a collapse dura-
 164 tion of 7 s, a collapse magnitude of 2.3 m, and a pressure increase of 1.7 MPa.

165 4 Discussion

166 4.1 Caldera collapse dynamics and model assumptions

167 In the idealized model, collapse dynamics is fully described by the characteristic
 168 length, time, pressure, and a dimensionless stress drop parameter (Appendix B), the re-
 169 lationships of which are akin to those proposed by Kumagai et al. (2001): larger cham-
 170 ber volume, higher total compressibility (magma+chamber), or larger caldera block mass,
 171 extends the duration of caldera collapse with a square root dependence, and increases
 172 total slip on the ring fault linearly. One contribution of this study is to recognize that,

173 downward displacement of the caldera block necessitates magma movement in the un-
 174 derlying chamber. The movement of magma imparts extra inertia to the caldera block
 175 (Eqn. 3 b), which slows its downward movement. Depending on the exact geometry of
 176 the magma chamber, the inertial effect may have varying degrees of importance. Future
 177 studies of caldera collapse should consider the inertial effects of magma movement on
 178 caldera collapse dynamics.

179 The model makes several assumptions regarding caldera collapse dynamics. No-
 180 tably, instantaneous drop in shear strength on the ring fault and negligible radiated en-
 181 ergy loss are assumed. The absence of pre-collapse acceleration of deformation suggests
 182 that the slip evolution distance, d_c , is less than 10 mm (Segall & Anderson, 2021). Com-
 183 pared with observed co-collapse slip of ~ 2.5 m, such d_c is consistent with an almost
 184 instantaneous drop in fault strength, leading to negligible fracture energy.

We assess the contribution of radiated energy to caldera collapse dynamics by com-
 185 paring the magnitude of the radiated energy, E_r (Eqn. 8), to the change in piston grav-
 186 itational potential, the dominant term in the piston-chamber energy balance (Eqn. S4).
 187 Energy, being quadratic in far-field velocities, does not obey superposition of radiated
 188 energy from moment and force sources calculated separately. However, given that our
 189 goal is to obtain an order of magnitude estimate, we simply add the two energies (deriva-
 190 tion in Appendix C):

$$\begin{aligned}
 E_r = & \frac{1}{60\pi\rho c_p^5} \int_0^\infty 3\ddot{M}_{xx}^2 + 3\ddot{M}_{yy}^2 + 3\ddot{M}_{zz}^2 + 2\ddot{M}_{xx}\ddot{M}_{yy} + 2\ddot{M}_{yy}\ddot{M}_{zz} + 2\ddot{M}_{xx}\ddot{M}_{zz} dt \\
 & + \frac{1}{30\pi\rho c_s^5} \int_0^\infty \ddot{M}_{xx}^2 + \ddot{M}_{yy}^2 + \ddot{M}_{zz}^2 - \ddot{M}_{xx}\ddot{M}_{yy} - \ddot{M}_{xx}\ddot{M}_{zz} - \ddot{M}_{yy}\ddot{M}_{zz} dt \\
 & + \frac{1}{12\pi\rho c_p^3} \int_0^\infty \dot{F}_z^2 dt \\
 & + \frac{1}{6\pi\rho c_s^3} \int_0^\infty \dot{F}_z^2 dt
 \end{aligned} \tag{8}$$

185 where c_p , c_s , ρ , are p-wave velocity, s-wave velocity, and crustal density. Here moment
 186 and force components are time dependent. Note that s-wave radiated energy for the mo-
 187 ment tensor vanishes in the isotropic limit ($\ddot{M}_{xx} = \ddot{M}_{yy} = \ddot{M}_{zz}$), as expected. The
 188 change in gravitational potential is $E_g = mg\Delta u$. For the MAP model at Kilauea, the
 189 radiated energy (2.2×10^{12} J) is $\sim 5\%$ the change in gravitational potential (3.5×10^{13}
 190 J). This justifies neglecting the radiated energy in the momentum balance (Eqn. 3), and
 191 is expected to hold true for other caldera collapses. Neglecting fracture and radiated en-
 192 ergy results in full dynamic overshoot. Thus, the quasi-dynamic shear stress decreases
 193 twice, at $t = 0$ and $t = t_{max}$ (Fig. 1 c), both of which are equal to the static-dynamic
 194 strength drop: $\Delta\tau_{str} = \tau_{str}^s - \tau_{str}^d = (f_s - f_d)\sigma_n$.

195 4.2 Coupled expansion source-single force and their contributions to ob- 196 servables

197 The tri-axial expansion source represents co-collapse pressurization of the cham-
 198 ber, contributing to both static and dynamic ground motions. Co-collapse inflation caused
 199 by chamber pressurization persists long after the end of each collapse event, because pres-
 200 sure reduction due to magma outflow occurs on a longer time scale than the collapse it-
 201 self. Therefore, in the point source representation, the moment tensor components of the
 202 expansion source have ramp-like time dependence (Fig. 1 d). Although the moment his-
 203 tory represents a monotonic increase in chamber pressure, convolution with elastodynamic
 204 Green's functions produces dynamic ground motions (Fig. 3 b).

205 The vertical single force represents momentum change of the caldera block/mobilized
 206 magma. It contributes to the dynamic ground motions, but not the static, extra-caldera
 207 inflationary deformation, in the limit of constant chamber mass during collapse. The sin-

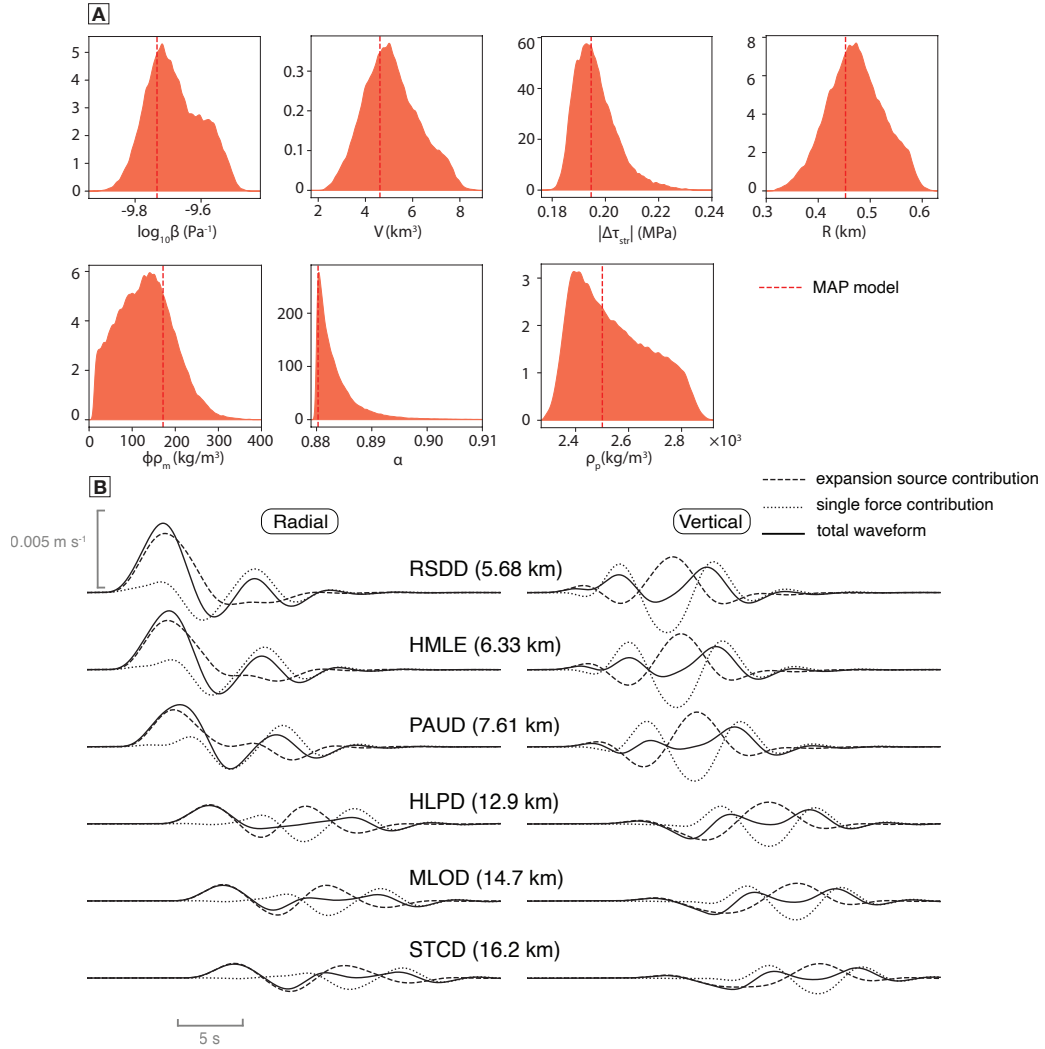


Figure 3: (a) Posterior probability density functions (PDFs) of the Bayesian Markov Chain Monte Carlo (MCMC) inversion after 1×10^6 iterations. MAP model denoted with vertical dashed line. (b) Moment tensor and vertical single force contributions to the synthetic velocity waveforms. Moment and single force contributions are comparable in magnitude. Individual components and total waveforms are low-pass filtered at 5 s.

208 gle force has significant contributions to the VLP waveforms. As shown in Fig. 3 b, for
 209 Kīlauea’s 2018 events and likely for caldera collapse in general, the magnitude of the sin-
 210 gle force contribution to the VLP waveform is comparable to the moment contribution.
 211 This demonstrates that, at least in the near field, kinematic moment tensor inver-
 212 sions not accounting for the single force could lead to biased results and interpretations. Fur-
 213 thermore, the single force and the expansion source are coupled through the pressure ex-
 214 erted at the bottom of the caldera block (Eqn. 3). Therefore, kinematic inversions that
 215 independently constrain moment tensors and single forces are inadequate in capturing
 216 the full caldera collapse dynamics.

Inversions accounting for both the expansion source and single force better con-
 strain parameter space, as demonstrated in the scaling of maximum pressure change δp_{max} ,
 and maximum vertical force $F_{z,max}$:

$$\delta p_{max} = -\frac{4L}{R}\Delta\tau_{str} \quad (9a)$$

$$F_{z,max} = \frac{2\pi RL}{\gamma}\Delta\tau_{str} \quad (9b)$$

217 where $\gamma = m'/m$. Therefore, a model that explains static displacement (only sensitive
 218 to δp_{max}) alone has complete trade off between L/R and $\Delta\tau_{str}$. A model that explains
 219 static/dynamic ground motions simultaneously is much better constrained. For instance,
 220 increasing $\Delta\tau_{str}$ from its optimum value would require a decrease in both RL/γ and L/R ,
 221 which can only be achieved by decrease L . Therefore, in practice, prior constraints on
 222 L would greatly enhance constraints on all parameters.

223 4.3 Analyses of Kīlauea’s 2018 caldera collapse

224 The near-field VLP waveforms at Kīlauea are highly sensitive to caldera-collapse
 225 dynamics (sensitivity analysis in Section S2). Among parameters that influence caldera
 226 collapse dynamics, co-collapse pressure increase and shear stress drop are of particular
 227 interest to hazard forecasting. The magnitude of co-collapse pressure increase influences
 228 the intensity of flank eruptions downstream of the reservoir (Patrick et al., 2019), whereas
 229 the magnitude of the shear stress drop is proportional to inter-collapse periods. At a 90%
 230 confidence interval, we estimate the co-collapse shear stress decrease by 0.37–0.42 MPa,
 231 with a corresponding pressure increase of 1.6–1.9 MPa, assuming MAP parameter value
 232 for R , V , and α (Table 1). Our inferred stress drop is higher than the 0.30–0.32 MPa
 233 reported by Roman and Lundgren (2021), although the pressure increase estimate is lower
 234 than the 3.3 MPa reported by Segall et al. (2019) for a vertical ring fault. The differ-
 235 ence between our estimated co-collapse pressure increase and that of Segall et al. (2019)
 236 can be reconciled when considering that the larger chamber volume and more oblate cham-
 237 ber geometry inferred here trade off with a smaller pressure increase. An oblate cham-
 238 ber geometry allows a smaller pressure increase to produce comparable vertical displace-
 239 ment at the surface, provided that misfit in radial displacement is not significantly im-
 240 pacted. However, the oblate chamber geometry is inconsistent with those inferred from
 241 pre- and post-collapse (Anderson et al., 2019; Wang et al., 2021) geodetic inversions, which
 242 indicate prolate chamber geometry. This discrepancy is not yet fully understood. The
 243 inferred piston radius, R , is in the range of 0.38 – 0.57 km, smaller than the 0.8 – 1.3
 244 km radii of the ring fault surface trace. This apparent discrepancy can be at least par-
 245 tially explained by the positive correlation between R and chamber volume, V , evident
 246 in both characteristic scales (Eqn. B1) and in correlation diagram (Fig. S7).

247 From the MAP model, we estimate that the mass of caldera block material involved
 248 in an average collapse is $\sim 1.6 \times 10^{12}$ kg. The inversion indicates that equivalent to \sim
 249 8×10^{11} kg of magma inertial mass was transiently mobilized by the descending caldera
 250 block, which represents $\sim 7\%$ of the inferred total magma mass in the Halema’ūma’u
 251 reservoir, assuming the MAP chamber volume of 4.6 km³ and bulk magma density of

252 2500 kg · m⁻³. Small mass fraction of mobilized chamber magma potentially reflects the
 253 complex geometry of the reservoir.

254 The proposed model provides a parsimonious explanation for both co-collapse static
 255 inflation and the VLP ground motions. Other potential mechanisms, such as slip on a
 256 non-vertical ring fault, have been suggested by moment tensor inversions (Lai et al., 2021)
 257 and theoretically shown to be resolvable at teleseismic distances (Sandambata et al., 2021).
 258 However, our model's accurate prediction of static displacement and VLP waveforms at
 259 Kīlauea suggest that, first order physics (caldera block/magma momentum change and
 260 chamber pressurization) likely dominates caldera collapse dynamics.

261 5 Conclusions

- 262 • A dynamic model based on first-order caldera collapse physics provides a parsimonious
 263 explanation for co-collapse static inflation and VLP ground motions
- 264 • Co-collapse static inflation reflects chamber pressurization (represented as tri-axial ex-
 265 pansion source), whereas VLP waveforms reflect time dependent caldera block/magma
 266 momentum change (represented as vertical single force), in addition to chamber
 267 pressurization
- 268 • Kinematic moment tensor or moment tensor + single force inversion can be biased given
 269 the coupled nature of expansion source and single force, whereas modeling of static
 270 displacement neglects additional constraints on parameter space due to caldera
 271 block/magma momentum change
- 272 • For an average caldera collapse event at Kīlauea in 2018, inversion suggests ring fault
 273 strength decrease of 0.19 MPa, chamber pressure increase of 1.7 MPa, mobilized
 274 crustal mass of 1.6×10^{12} kg, and mobilized magmatic inertial mass of 8×10^{11}
 275 kg.

276 Acknowledgement

277 This project was supported by National Science Foundation (NSF) grant EAR-2040425
 278 and EAR-1930979.

279 Data Availability Statement

280 GNSS data are available through UNAVCO archive (<https://www.unavco.org/data/data.html>).
 281 Accelerometer and broadband data are available through the Incorporated Research In-
 282 stitute for Seismology (IRIS) Data Management Center ([http://ds.iris.edu/ds/nodes/dmc/data/types/waveform-](http://ds.iris.edu/ds/nodes/dmc/data/types/waveform-data/)
 283 [data/](http://ds.iris.edu/ds/nodes/dmc/data/types/waveform-data/)).

284 Appendix A Effect of magma inertia on acoustic impedance

285 A 1D analysis for the effective impedance of the chamber generates insight of magma
 286 inertial effect on piston movement, neglecting fluid viscosity. We consider a vertically
 287 oriented, cylindrical chamber of length, H , and cross sectional area, \mathcal{A} . The chamber has
 288 rigid walls, and is filled with compressible magma. The base of the piston is at $z = 0$
 289 (same coordinate system as in Fig. 1 b). Fluid particle motion is constrained to the z
 290 direction. The goal is to obtain a relationship between magma inertia, magma storativ-
 291 ity, and chamber pressure.

In the frequency domain, the plane wave solution for pressure perturbation is:

$$\delta\hat{p}(z, \omega) = \hat{a} \cos\left(\frac{\omega z}{c}\right) + \hat{b} \sin\left(\frac{\omega z}{c}\right) \quad (\text{A1})$$

where c is magma acoustic wave speed. \hat{a} and \hat{b} are unknown coefficients determined by boundary conditions. Substitute pressure perturbation into the Euler equation in the

frequency domain, $\rho\omega\hat{v} = \partial\hat{p}/\partial z$ (note the material derivative in the Euler equation is simplified to a time derivative due to the large magnitude of acceleration compared to spatial variations in particle velocity), we obtain particle velocity:

$$\hat{v}(z, \omega) = \frac{i\hat{a}}{\rho c} \sin\left(\frac{\omega z}{c}\right) - \frac{i\hat{b}}{\rho c} \cos\left(\frac{\omega z}{c}\right) \quad (\text{A2})$$

Apply the zero velocity boundary condition at $z = H$ yields $\hat{b} = \hat{a} \tan(\omega H/c)$. Next compute the hydraulic impedance (ratio of perturbation pressure over volume flow rate), \hat{Z} , at $z = 0$. The sine terms vanish at $z = 0$, and the result depends on \hat{b}/\hat{a} :

$$\hat{Z}(0, \omega) = \frac{\delta\hat{p}(0, \omega)}{\hat{v}(0, \omega)\mathcal{A}} = \frac{\rho c}{-i \tan(\frac{\omega H}{c})\mathcal{A}} \quad (\text{A3a})$$

$$\cot\left(\frac{\omega H}{c}\right) = \frac{c}{\omega H} + \frac{\omega H}{3c} - \frac{1}{45}\left(\frac{\omega H}{c}\right)^3 \quad (\text{A3b})$$

We expand the cotangent term in the impedance with regard to $\omega H/c$ using Taylor series and keep terms up to order two, justified in the low frequency limit. We then recognize the chamber storativity, $S = (\mathcal{A}H)/\rho c^2 = \beta_m V$, and fluid mass, $m_f = \rho H\mathcal{A}$, embedded in the impedance expression:

$$\hat{Z}(0, \omega) = \frac{i\rho c^2}{\mathcal{A}\omega H} - \frac{i\rho\omega H}{3\mathcal{A}} \quad (\text{A4a})$$

$$= \frac{1}{-i\omega S} + \frac{-i\omega m_f}{3\mathcal{A}^2} \quad (\text{A4b})$$

We can now invert the impedance to time domain:

$$\delta\hat{p} = \left(\frac{1}{-i\omega S} + \frac{-i\omega m_f}{3\mathcal{A}^2}\right)\hat{v}\mathcal{A} \quad (\text{A5a})$$

$$-i\omega\delta\hat{p}S = \left(1 + \frac{(-i\omega)^2 m_f S}{3\mathcal{A}^2}\right)\hat{v}\mathcal{A} \quad (\text{A5b})$$

$$S\frac{\partial\delta p}{\partial t} = v\mathcal{A} + \frac{m_f S}{3\mathcal{A}}\frac{\partial^2 v}{\partial t^2} \quad (\text{A5c})$$

$$\frac{\partial\delta p}{\partial t} = \frac{v\mathcal{A}}{S} + \frac{m_f}{3\mathcal{A}}\frac{\partial^2 v}{\partial t^2} \quad (\text{A5d})$$

The above equation indicates that, the downward displacement is impeded by not only the storativity of the chamber, but the inertia of the magma. Integrating both sides of Eqn. A5d in time, we obtain:

$$p = \frac{\pi R^2}{\beta_m V}u + \frac{m_f}{3\mathcal{A}}\frac{\partial^2 u}{\partial t^2} + p_0 \quad (\text{A6})$$

292 where β_m is the compressibility of the magma. More generally, a linearization of the mass
 293 conservation equation for chambers of arbitrary geometry (e.g., Segall et al., 2001) leads
 294 to $\frac{\pi R^2}{\beta V}u$, where β is the total compressibility. The inertial correction in the above equation
 295 can be generalized to chambers of arbitrary geometry, provided that the factor of
 296 $1/3$ be replaced by an appropriate one.

297 Appendix B non-dimensional solutions

To better understand the dynamics, we nondimensionalize Eqn. 3 using the following characteristic time, pressure, and length:

$$t^* = \sqrt{\frac{\beta V m'}{\pi^2 R^4}} \quad (\text{B1a})$$

$$p^* = \frac{m' g}{\pi R^2} \quad (\text{B1b})$$

$$l^* = \frac{\beta V m' g}{\pi^2 R^4} \quad (\text{B1c})$$

The momentum balance equation then becomes:

$$\ddot{\hat{u}} + \hat{u} = \pi_0 \quad (\text{B2a})$$

$$\pi_0 = \frac{1}{m'g} (mg - 2\pi RL\tau_{str}^d - \pi R^2 p_0) = -\frac{2\pi RL}{m'g} \Delta\tau_{str} \quad (\text{B2b})$$

298 π_0 can be understood as the dimensionless magnitude of shear strength drop.

Setting initial displacement and velocity to zero, we solve the dimensionless momentum equation:

$$\hat{u} = \pi_0(1 - \cos \hat{t}) \quad (\text{B3a})$$

$$\delta\hat{p} = \hat{u} \quad (\text{B3b})$$

where we omit the spatially dependent inertial correction to the perturbation pressure due to the lumped parameter nature of the model. It follows that the duration and magnitude of collapses are:

$$\hat{t}_{max} = \pi \quad (\text{B4a})$$

$$\hat{u}_{max} = 2\pi_0 \quad (\text{B4b})$$

299 **Appendix C Radiated energy from point source representation**

We can compute the radiated energy from the point source representation, assuming homogeneous full space. The energy rate can be expressed as the integral of far field particle velocity with traction in the same direction over a sphere enclosing the source, following Aki and Richards (2002):

$$\dot{E}_{radiation} = \oint\!\!\!\oint v_i \sigma_{ij} n_j dS \quad (\text{C1})$$

where $i, j = 1, 2, 3$, or equivalently, x, y, z . Note here the integration is over a sphere at radius r centered at the source ξ_i . n_j denotes the surface normal vector. Without loss of generality, let $\xi_i = [0, 0, 0]$ for convenience. Substitute traction $\sigma_{ij} n_j$ with the product of specific impedance and far field particle velocity yields:

$$\dot{E}_{radiation} = \oint\!\!\!\oint v_i \rho c v_i dS \quad (\text{C2})$$

300 where c is either p-wave or s-wave velocity.

We then substitute in far-field p-wave and s-wave velocity induced by a point source moment tensor and a single force (Aki & Richards, 2002):

$$v_n^{m,p} = \frac{\gamma_n \gamma_p \gamma_q}{4\pi \rho c_p^3} \frac{1}{r} \ddot{M}_{pq} \left(t - \frac{r}{c_p}\right) \quad (\text{C3a})$$

$$v_n^{m,s} = -\left(\frac{\gamma_n \gamma_p - \delta_{np}}{4\pi \rho c_s^3}\right) \gamma_q \frac{1}{r} \ddot{M}_{pq} \left(t - \frac{r}{\beta}\right) \quad (\text{C3b})$$

$$v_n^{f,p} = \frac{1}{4\pi \rho c_p^2} \gamma_n \gamma_p \frac{1}{r} \dot{F}_p \left(t - \frac{r}{c_p}\right) \quad (\text{C3c})$$

$$v_n^{f,s} = -\frac{1}{4\pi \rho c_s^2} (\gamma_n \gamma_p - \delta_{np}) \frac{1}{r} \dot{F}_p \left(t - \frac{r}{\beta}\right) \quad (\text{C3d})$$

301 where the directional cosines are defined as $\gamma_i = (x_i - \xi_i)/|x_i - \xi_i|$. Superscripts m, f,
302 p, s denote moment tensor source, single force source, p-wave, and s-wave, respectively.
303 Source receiver distance is labeled as $r = |x_i - \xi_i|$. c_p and c_s are p-wave and s-wave
304 velocities.

Given the assumption that spheroid chamber has its axes aligned with the axes of the coordinate system, the moment tensor is diagonalized. Also here only vertical single force is considered. These two assumptions greatly simplify the integration kernels for radiated energy rate:

$$\begin{aligned}
 v_i^{m,p} v_i^{m,p} &= \frac{1}{16\pi^2 \rho^2 c_p^6 R^2} (\gamma_1^2 \ddot{M}_{11} + \gamma_2^2 \ddot{M}_{22} + \gamma_3^2 \ddot{M}_{33})^2 \\
 v_i^{m,s} v_i^{m,s} &= \frac{1}{16\pi^2 \rho^2 c_s^6 R^2} [\ddot{M}_{11}^2 (-\gamma_1^4 + \gamma_1^2) + \ddot{M}_{22}^2 (-\gamma_2^4 + \gamma_2^2) + \ddot{M}_{33}^2 (-\gamma_3^4 + \gamma_3^2) \\
 &\quad + \ddot{M}_{11} \ddot{M}_{22} (-2\gamma_1^2 \gamma_2^2) + \ddot{M}_{11} \ddot{M}_{33} (-2\gamma_1^2 \gamma_3^2) + \ddot{M}_{22} \ddot{M}_{33} (-2\gamma_2^2 \gamma_3^2)] \\
 v_i^{f,p} v_i^{f,p} &= \frac{1}{16\pi^2 \rho^2 c_p^4 R^2} (\gamma_3 \dot{F}_3)^2 \\
 v_i^{f,s} v_i^{f,s} &= \frac{1}{16\pi^2 \rho^2 c_s^4 R^2} (-\gamma_3^2 + 1) \dot{F}_3^2
 \end{aligned}$$

The integration over the sphere benefits from the following Cartesian-spherical coordinate conversion: $\gamma_1 = \cos \theta \cos \phi$, $\gamma_2 = \cos \theta \sin \phi$, $\gamma_3 = \sin \theta$. Assuming a positive z axis in the vertical direction, θ is measured from negative z-axis to positive z-axis (0 to π) and ϕ counterclockwise from positive x-axis (0 to 2π). Lastly, integrate the radiation rate over time yields the total energy (Eqn. 8).

References

- Aki, K., & Richards, P. G. (2002). Quantitative seismology. In (p. 76-77). Sausalito, California: University Science Books.
- Anderson, K., Johanson, I., Patrick, M. R., Gu, M., Segall, P., Poland, M., ... Miklius, A. (2019). Magma reservoir failure and the onset of caldera collapse at Kilauea volcano in 2018. *Science*, *366*(6470).
- Anderson, K., & Poland, M. (2016). Bayesian estimation of magma supply, storage, and eruption rates using a multiphysical volcano model: Kilauea volcano, 2000–2012. *Earth and Planetary Science Letters*, *447*, 161–171.
- Cervelli, P. (2013). Analytical expressions for deformation from an arbitrarily oriented spheroid in a half-space. *American Geophysical Union, Fall Meeting abstract*, *V44C-06*.
- Davis, P. M. (1986). Surface deformation due to inflation of an arbitrarily oriented triaxial ellipsoidal cavity in an elastic half-space, with reference to Kilauea volcano, Hawaii. *Journal of Geophysical Research: Solid Earth*, *91*(B7), 7429–7438.
- Duputel, Z., & Rivera, L. (2019). The 2007 caldera collapse of Piton de la Fournaise volcano: Source process from very-long-period seismic signals. *Earth and Planetary Science Letters*, *527*, 115786.
- Eshelby, J. D. (1957). The determination of the elastic field of an ellipsoidal inclusion, and related problems. *Proceedings of the royal society of London. Series A. Mathematical and physical sciences*, *241*(1226), 376–396.
- Fontaine, F. R., Roult, G., Hejrani, B., Michon, L., Ferrazzini, V., Barruol, G., ... others (2019). Very-and ultra-long-period seismic signals prior to and during caldera formation on La Réunion island. *Scientific reports*, *9*(1), 1–15.
- Foreman-Mackey, D., Hogg, D. W., Lang, D., & Goodman, J. (2013). emcee: The mcmc hammer. *Publications of the Astronomical Society of the Pacific*, *125*(925), 306.
- Gudmundsson, M. T., Jónsdóttir, K., Hooper, A., Holohan, E. P., Halldórsson, S. A., Ófeigsson, B. G., ... others (2016). Gradual caldera collapse at Bárðarbunga volcano, Iceland, regulated by lateral magma outflow. *Science*, *353*(6296).

- 342 Kumagai, H., Ohminato, T., Nakano, M., Ooi, M., Kubo, A., Inoue, H., & Oikawa,
343 J. (2001). Very-long-period seismic signals and caldera formation at Miyake
344 Island, Japan. *Science*, *293*(5530), 687–690.
- 345 Lai, V. H., Zhan, Z., Sandanbata, O., Brissaud, Q., & Miller, M. S. (2021). Inflation
346 and asymmetric collapse at Kilauea summit during the 2018 eruption from
347 seismic and infrasound analyses.
- 348 Michon, L., Villeneuve, N., Catry, T., & Merle, O. (2009). How summit calderas
349 collapse on basaltic volcanoes: new insights from the April 2007 caldera col-
350 lapse of Piton de la Fournaise volcano. *Journal of Volcanology and Geothermal*
351 *Research*, *184*(1-2), 138–151.
- 352 Patrick, M. R., Dieterich, H. R., Lyons, J. J., Diefenbach, A. K., Parcheta, C., An-
353 derson, K., . . . Kauahikaua, J. P. (2019). Cyclic lava effusion during the 2018
354 eruption of Kilauea volcano. *Science*, *366*(6470).
- 355 Roman, A., & Lundgren, P. (2021). Dynamics of large effusive eruptions driven by
356 caldera collapse. *Nature*, *592*(7854), 392–396.
- 357 Sandanbata, O., Kanamori, H., Rivera, L., Zhan, Z., Watada, S., & Satake, K.
358 (2021). Moment tensors of ring-faulting at active volcanoes: Insights into
359 vertical-clvd earthquakes at the Sierra Negra caldera, Galápagos Islands. *Jour-*
360 *nal of Geophysical Research: Solid Earth*, e2021JB021693.
- 361 Segall, P., & Anderson, K. (2021). Repeating caldera collapse events constrain
362 fault friction at the kilometer scale. *Proceedings of the National Academy of*
363 *Sciences*, *118*(30).
- 364 Segall, P., Anderson, K., Johanson, I., & Miklius, A. (2019). Mechanics of infla-
365 tionary deformation during caldera collapse: Evidence from the 2018 Kilauea
366 eruption. *Geophysical Research Letters*, *46*(21), 11782–11789.
- 367 Segall, P., Anderson, K., Pulvirenti, F., Wang, T., & Johanson, I. (2020). Caldera
368 collapse geometry revealed by near-field GPS displacements at Kilauea volcano
369 in 2018. *Geophysical Research Letters*, *47*(15), e2020GL088867.
- 370 Segall, P., Cervelli, P., Owen, S., Lisowski, M., & Miklius, A. (2001). Constraints
371 on dike propagation from continuous gps measurements. *Journal of Geophysi-*
372 *cal Research: Solid Earth*, *106*(B9), 19301–19317.
- 373 Wang, T., Zheng, Y., Pulvirenti, F., & Segall, P. (2021). Post-2018 caldera collapse
374 re-inflation uniquely constrains Kilauea’s magmatic system. *Journal of Geo-*
375 *physical Research. Solid Earth*, *126*, e2021JB021803.
- 376 Yang, X.-M., Davis, P. M., & Dieterich, J. H. (1988). Deformation from inflation of
377 a dipping finite prolate spheroid in an elastic half-space as a model for volcanic
378 stressing. *Journal of Geophysical Research: Solid Earth*, *93*(B5), 4249–4257.
- 379 Zhu, L., & Rivera, L. A. (2002). A note on the dynamic and static displacements
380 from a point source in multilayered media. *Geophysical Journal International*,
381 *148*(3), 619–627.